Optics Letters

Thermo-optic coefficient of PECVD silicon-rich silicon nitride

Natale G. Pruiti,[1,*] Charalambos Klitis,[1] Christopher Gough,[1] Stuart May,[1] and Marc Sorel[1,2]

[1]School of Engineering, University of Glasgow, Glasgow, G12 8LT, UK
[2]Institute of Technologies for Communication, Information and Perception (TeCIP), Sant'Anna School of Advanced Studies, Via Moruzzi 1, 56127 Pisa, Italy
*Corresponding author: n.pruiti.1@research.gla.ac.uk

Received 5 August 2020; revised 10 September 2020; accepted 4 October 2020; posted 5 October 2020 (Doc. ID 403357); published 12 November 2020

The thermo-optic coefficient (TOC) of photonic integrated waveguides fabricated on silicon-rich silicon nitride grown by plasma-enanched chemical vapor deposition is characterized for the first time, to the best of our knowledge. The TOC is found to increase linearly with the fractional composition of silicon over a range from that of silicon nitride to a-Si. This finding is significant for improving the power efficiency of thermally tuned photonic integrated circuits.

https://doi.org/10.1364/OL.403357

Silicon nitride (SiN) is a well-established CMOS-compatible material platform for photonic integrated circuits (PICs) [1]. The combination of its large bandgap with very low waveguide propagation losses [2] makes it an ideal platform for the development of PICs for a large range of applications in optical atomic clocks, atom cooling, biosensing, and precision spectroscopy [2]. Also, the absence of two-photon absorption (TPA) in the near infrared (IR) wavelength range [3] provides a distinct advantage over Si-based platforms for which TPA is a major hindrance. This fundamental property of SiN led to the demonstration of several nonlinear optical PICs such as ultra-narrowband Brillouin lasers [4], waveguides for supercontinuum generation (SCG) spanning from the visible to the mid-IR [5], and microresonators for mode-locked ultrashort pulse generation [6] and octave-spanning dissipative Kerr soliton frequency comb generation [7].

Despite the many achievements of SiN, however, the low refractive index contrast between the core and cladding layers ($\Delta n \approx 0.55$) results in an increased device footprint with respect to the Si-on-insulator (SOI) platform. Circuit tunability is also a problem in SiN devices. In fact, many applications, such as all-optical switching [8], optical modulators [9], and frequency comb generation [10], often rely on the possibility to dynamically tune and control the optical properties of a PIC. A popular way to achieve the desired tunability is based on the thermo-optic (TO) effect. The efficiency of the thermal tuning depends on the TO coefficient (TOC) $K = \partial n/\partial T$ of the material, which describes the change in its refractive index n with respect to a change in temperature T. The sign and magnitude of the TOC are determined by how the density and polarizability of a material change with temperature [11]. As the TOC of SiN ($K \approx 2 \cdot 10^{-5}{}^{\circ}\mathrm{C}^{-1}$ [12]) is significantly lower than that of both crystalline Si ($K_{c-\mathrm{Si}} = 18.5 \cdot 10^{-5}{}^{\circ}\mathrm{C}^{-1}$ [13]) and amorphous Si (ranging from $K_{a-\mathrm{Si}} \approx 16 \cdot 10^{-5}{}^{\circ}\mathrm{C}^{-1}$ to $\approx 24 \cdot 10^{-5}{}^{\circ}\mathrm{C}^{-1}$ depending on the hydrogenation of the film [14]), the thermal tuning in SiN-based devices is inefficient. This low TOC ultimately results in a higher electrical power consumption required for tuning (up to hundreds of milliwatt per device), a larger footprint, and faster deterioration [15].

One possible solution to address this issue is Si-rich SiN (SRSN). Initially developed to reduce the high stress of SiN films [16], SRSN has recently attracted substantial interest as a PIC platform, as it offers the unique prospect to tailor its optical properties between that of SiN and amorphous Si [17]. Simply by changing the growth parameters, the percentage of Si in the material can be increased, making it possible to tune both its linear and nonlinear refractive indices [18]. Not only does SRSN provide a powerful route to engineer the optimal waveguide index contrast for a given application, but it also exhibits a substantial increase in the third-order nonlinear coefficient of the material, which has already resulted in the demonstration of SRSN PICs for high parametric gain [19], broadband SCG [20], and highly efficient nonlinear all-optical signal processing [21].

While the effects of increasing the Si content in SRSN on the linear and nonlinear refractive indices have been extensively studied, little is known about how the Si concentration affects the TOC. Lim *et al*. [22] first reported the TOC of a SRSN film grown by inductively coupled plasma chemical vapor deposition (ICP-CVD). Continuing on from this work, we present for the first time a systematic characterization of the TOC of plasma-enanched CVD (PECVD) SRSN with different Si compositions. We use a combination of microresonator and straight

waveguide interferometric measurements at different temperatures to characterize the materials, and demonstrate that, much like the refractive index, the TOC can also be tailored between that of stoichiometric SiN and amorphous Si.

For this work, films with a thickness of 500 nm were deposited by PECVD onto a Si wafer with a 3 μm thick buried oxide layer. The deposition was carried out with an SPTS Delta PECVD tool, using a NH_3-free recipe for stoichiometric SiN suggested by the manufacturer as a starting point, with a $SiH_4 : N_2$ chemistry (100:3000 sccm), a radio frequency (RF) generator power of 1200 W, and chamber pressure of 2200 mTorr. By decreasing the platen power during the deposition, four different compositions, with a refractive index extending from 2.26 to 2.73 measured by ellipsometry, were obtained and used for the TOC analysis of the material. The bond composition of each film was calculated through Fourier-transform IR spectroscopy (FTIR) measurements as described in [23], giving a N:Si ratio x of 0.39–1.03 for the refractive index range considered (see Table 1). The devices were then patterned by electron-beam lithography using a hydrogen silsesquioxane (HSQ) mask and transferred to the SRSN by an ICP-reactive ion etching (RIE) SF_6/C_4F_8 dry etching chemistry. The waveguides were deep etched to the silica cladding as illustrated by the schematic in Fig. 1(a). The samples were finally coated with a 1 μm thick layer of HSQ, and cured at 180°C for 24 h to form a SiO_x-like material with a refractive index of 1.39.

Table 1. Refractive Indices n at $\lambda = 1550$ nm, and N:Si Ratios x of the Four SRSN Material Platforms Used in This Study (data for stoichiometric SiN also reported for comparison)

Material	n	x
Si_3N_4 [12]	1.97	1.33
$SRSN_1$	2.26	1.03
$SRSN_2$	2.34	0.98
$SRSN_3$	2.54	0.68
$SRSN_4$	2.73	0.39

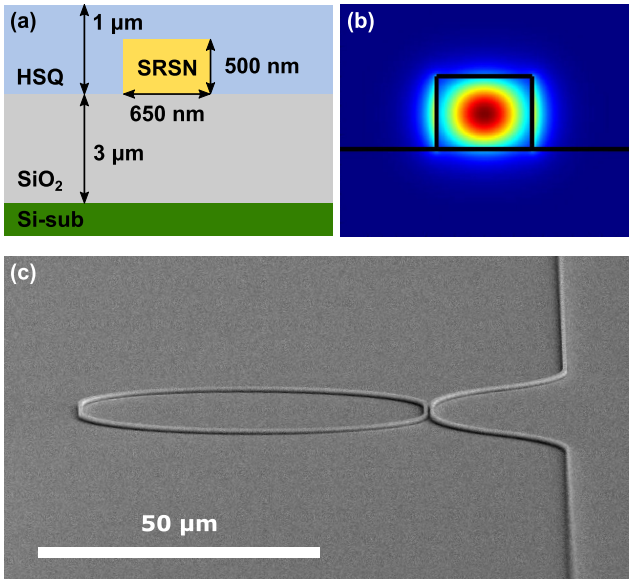

Fig. 1. (a) Schematic cross section of the SRSN waveguides, (b) simulated modal field intensity distribution in a waveguide with a width of 650 nm and fabricated on the $SRSN_1$ material, and (c) SEM image of a fabricated SRSN racetrack microring resonator.

The fabricated devices included sets of waveguides with different widths and microring resonators. For a width up to 650 nm, measurements indicated single-mode propagation at a wavelength of 1550 nm for all four SRSN materials listed in Table 1. For such a waveguide width the confinement factor ranges from 77% for $SRSN_1$ to 90% for $SRSN_4$.

Transmission spectrum measurements were performed by end-fire coupling the light emitted by a tuneable CW semiconductor laser into the waveguides through a polarization maintaining (PM) lensed fiber, while a 20× microscope objective was used to collimate the output beam. An in-line fibre polarizer and a polarization controller were used to ensure that only the fundamental quasi-transverse electric (TE) mode was excited in the waveguide. The signal, modulated by a chopper blade, was then measured using an InGaAs photodetector and a lock-in amplifier. Each sample was mounted onto a stage whose temperature was controlled by a thermo-electric cooler module with an accuracy of 0.01°C.

The use of resonant cavities provides a very precise and accurate method for the measurement of the TOC in waveguide devices [24]. The wavelength shift $\Delta\lambda$ of the resonant frequency of a resonator produced by a change in temperature ΔT_R is given by a combination of a change in the effective index n_{eff} due to the TO effect and to the thermal expansion of the substrate [25]:

$$\Delta\lambda = \left(\frac{\partial n_{\text{eff}}}{\partial T_R} + n_{\text{eff}} \cdot \alpha_{\text{sub}}\right) \frac{\lambda}{n_g} \Delta T_R, \tag{1}$$

where λ is the resonance wavelength before the temperature change, α_{sub} is the thermal linear expansion coefficient of the substrate, and n_g is the group index given by [26]

$$n_g = n_{\text{eff}} - \lambda \frac{\partial n_{\text{eff}}}{\partial \lambda} = \frac{\lambda^2}{L_R \cdot \text{FSR}}, \tag{2}$$

with L_R and FSR being the resonator length and the free spectral range, respectively. Equation (1) is valid for any type of resonator provided the appropriate values of L_R and FSR are used in Eq. (2).

Differentiating Eq. (1) with respect to temperature, an effective TOC K_{eff} can be defined as [15]

$$K_{\text{eff}} = \frac{\partial n_{\text{eff}}}{\partial T_R} = \frac{n_g}{\lambda} \frac{\partial \lambda}{\partial T_R} - n_{\text{eff}} \cdot \alpha_{\text{sub}}, \tag{3}$$

where $\partial\lambda/\partial T_R$ is the temperature-dependent wavelength shift (TDWS). Because the effective TOC is the result of the interaction of the mode with the waveguide core and cladding layers, it can be written as [15]

$$K_{\text{eff}} = \sum_i K_i \Gamma_i, \tag{4}$$

where K_i is the TOC of the ith material, and Γ_i is the confinement factor of the optical mode in that material. If the TOCs of all the cladding layers are known, Eq. (4) can be used to calculate the TOC of the SRSN material under test. Generally, the dependence of the material refractive index with temperature is nonlinear and varies with wavelength, resulting in a temperature and wavelength dependent TOC. However, because of the small

temperature and wavelength ranges involved in this study, this dependence can be assumed to be linear.

To ensure a good accuracy of the TOC measurements, the system was first calibrated using an SOI microring with 2 μm thick buried SiO_2 layer and upper HSQ cladding, whose core TOC is well known ($K_{c-Si} = 18.5 \cdot 10^{-5}°C^{-1}$ [13]). The calibration takes in account both the error between the thermistor reading and the actual temperature of the Peltier cell, and the temperature difference between the Peltier cell and the waveguide. The latter is due to the thermal resistivity of the different materials and depends on many factors such as the ambient temperature, the thicknesses of the sample Si substrate and SiO_2 layer, and the adhesion between the sample and the thermally controlled stage. Nonetheless, in our laboratory controlled environment (i.e., constant ambient temperature at 18°C), and for the small temperature range involved in this study (i.e., from 20°C to 30°C), the effects of the ambient temperature and variation of the buried oxide thickness are negligible compared to the error between the thermistor reading and the actual temperature of the Peltier cell. This resulted in a calibration factor $T_{cal} = 1.2 \pm 0.1$, such that the temperature T_M measured on the Peltier cell by a thermistor is related to the real waveguide temperature T_R by the equation $T_R = T_{cal} \cdot T_M$.

For each of the SRSN material platforms, the transmission spectra of the microring resonators for the fundamental TE mode were measured, across a range between 20°C and 30°C, as illustrated in Fig. 2. By performing a linear fitting of the resonance position against the resonator temperature, the TDWS $\partial\lambda/\partial T_R$ was calculated taking into account the uncertainty on the calibration factor T_{cal}. Using Eq. (3), the effective TOC K_{eff} was then obtained, and finally the TOC of each SRSN sample was calculated through Eq. (4), where modal effective indices n_{eff} and confinement factors Γ were obtained through finite difference simulations, $\alpha_{sub} = 2.6 \cdot 10^{-6}$ [27], and $K_{SiO_2} = 1 \cdot 10^{-5}°C^{-1}$ [12] at 1550 nm. The TOC of HSQ was obtained through the characterization of the same SOI microring used for the calibration of the system. In order to do so, both fundamental quasi-TE and quasi-transverse magnetic (TM) transmissions were measured. As the two modes present different confinement factors, this provides a set of two independent equations that can be used to calculate the calibration factor T_{cal} and the TOC of HSQ K_{HSQ} at the same time, resulting in $K_{HSQ} = 1 \cdot 10^{-5}°C^{-1}$. For the curing temperature and time used in this work, the HSQ TOC value was found to be identical to that of PECVD silica; however, it should be noted that the thermal properties of HSQ can vary substantially depending on the curing conditions [28].

Similar TOC values were found by measuring the shift of the Fabry–Perot (FP) fringes in straight waveguides. It is worth noting, however, that while straight waveguides are easier to fabricate and, in our case, provided the same results as microring resonators, they also come with two important limitations. The cavity is formed by the reflection that arises from the cleaved edges of the chip. Because the minimum length of cleaved chips is typically limited to a few millimeters, the FSR does not exceed a few tens of gigahertz, which may lead to ambiguity in tracking the resonant peaks in situations that cause shifts over multiple FSRs. Also, without any additional high reflection (HR) coatings deposited on the cleaved facets, the reflectivities are in the range 15%–22% (depending on the refractive index of the SRSN waveguide), which leads to low Q-factor values and therefore to little precision when smaller wavelength shifts are to be measured. Because short cavity lengths and high Q-factors can be easily defined by adjusting the device design, microring resonators are more suitable options for high precision measurements or large refractive index shifts [24].

The measured TOCs plotted against the N:Si ratio of the different materials are shown in Fig. 3, where the fitting shows a linear increase of the TOC on the Si concentration. These results are consistent with other studies on SRSN, where linear and nonlinear refractive indices have also been found to increase with the Si content in the material [17,19]. From the experimental data, an empirical expression for the TOC of SRSN K_{SRSN} as a function of the N:Si ratio x can be derived as

$$K_{SRSN}(x) = 14.71 - 10.33 \cdot x, \tag{5}$$

with $K_{SRSN}(x)$ expressed in $10^{-5}°C^{-1}$ units.

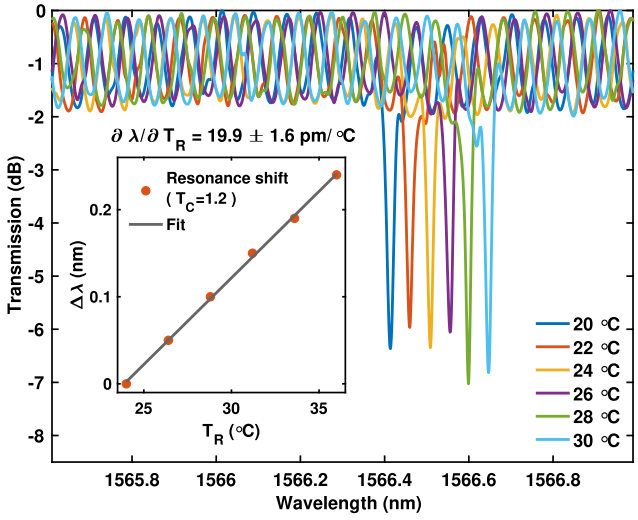

Fig. 2. Spectral response of a SRSN resonator at different measured temperatures. The resonance wavelength shift Δλ against the waveguide temperature T_R is illustrated in the inset.

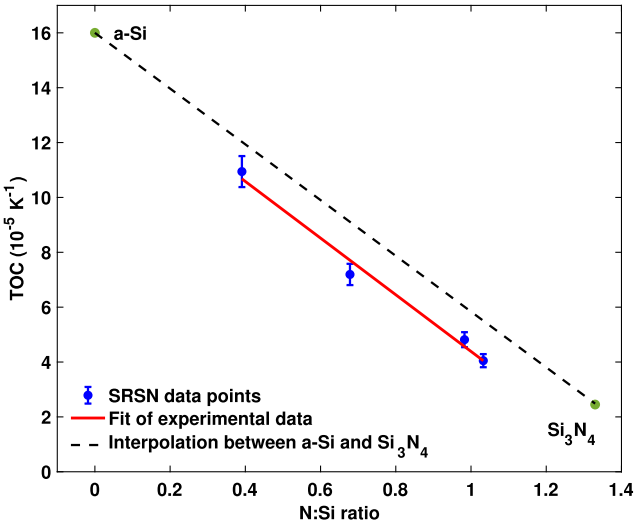

Fig. 3. Measured TOCs plotted against the N:Si ratio of the material. The red line is the linear fitting of the measured data, while the black dashed line is a linear interpolation between the TOCs of amorphous silicon ($K_{a-Si} = 16 \cdot 10^{-5}°C^{-1}$ [14]) and stoichiometric SiN ($K_{Si_3N_4} = 2.45 \cdot 10^{-5}°C^{-1}$ [12]), also reported for reference.

The linear interpolation between the TOC values of amorphous Si and stoichiometric SiN found in the literature is also reported in Fig. 3 as a guide for the eyes. When our expression is compared to these data, we find that they differ by $1.4 \cdot 10^{-5}{}^{\circ}\mathrm{C}^{-1}$ across the whole measured range.

A possible explanation for this discrepancy can be related to the fact that the N:Si ratio x in the material is the only parameter considered in this analysis. In fact, the origin of the TOC is far more complex, and is related to two main factors: the thermal expansion, and the thermal occupancies and spectra of the material energy levels [11]. The latter is the dominant factor in positive-TOC materials, and is in turn dominated by the bandgap. Specifically, for a small temperature change, Ghosh's model [29] shows a linear dependence with the inverse of the excitonic bandgap. Our results are consistent with this model, as the increment of Si in the SRSN film results in a reduction of the bandgap [18]. However, the bandgap of an amorphous material is actually influenced by many factors, such as the state of disorder, the hydrogen content, and the bond configurations within the material [30], to the point that different deposition techniques can yield different bandgap values for the same material [31]. For instance, Zhou *et al*. reported an increment in the TOC of hydrogenated amorphous Si as the concentration of Si–H bonds in the film was increased [14]. Therefore, the reason for the difference between our data and those obtained by interpolating the TOC values of amorphous Si and stoichiometric SiN could lie in the different deposition techniques and recipes used. In fact, while for the preparation of the material involved in this study we exploited an NH_3-free PECVD recipe, aimed at minimizing the presence of N–H bonds in the films, the reported TOC of stochiometric SiN has been measured on a film grown by low-pressure CVD (LPCVD) [32].

In conclusion, the TOC of SRSN with different levels of Si concentration was characterized by measuring the TDWS $\partial\lambda/\partial T_R$ of waveguide resonators. The TOC has been found to increase linearly with the Si concentration in the material. Specifically, experimental data showed that the TOC could be increased by nearly threefold, from $4 \cdot 10^{-5}{}^{\circ}\mathrm{C}^{-1}$ to $11 \cdot 10^{-5}{}^{\circ}\mathrm{C}^{-1}$, by varying the platen power during the PECVD deposition. These results provide a deeper understanding of how the material properties change with its composition. This finding is of great importance to reduce the power consumption for thermal tuning in SiN-based PICs, thus paving the way for more complex designs with higher component density and higher tuning efficiency.

Funding. Engineering and Physical Sciences Research Council (EP/L015323/1, EP/P005624/1); H2020 Future and Emerging Technologies (829116).

Acknowledgment. The authors acknowledge the technical staff at the James Watt Nano-fabrication Centre at Glasgow University. N. G. Pruiti gratefully acknowledges studentship funding support from Fraunhofer UK.

Disclosures. The authors declare no conflicts of interest.

REFERENCES

1. D. J. Moss, R. Morandotti, A. L. Gaeta, and M. Lipson, Nat. Photonics **7**, 597 (2013).
2. D. J. Blumenthal, APL Photon. **5**, 020903 (2020).
3. J. Bauters, M. Heck, D. John, D. Dai, M.-C. Tien, J. Barton, A. Leinse, R. Heideman, D. Blumenthal, and J. Bowers, Opt. Express **19**, 3163 (2011).
4. S. Gundavarapu, G. M. Brodnik, M. Puckett, T. Huffman, D. Bose, R. Behunin, J. Wu, T. Qiu, C. Pinho, N. Chauhan, J. Nohava, P. T. Rakich, K. D. Nelson, M. Salit, and D. J. Blumenthal, Nat. Photonics **13**, 60 (2019).
5. M. A. G. Porcel, F. Schepers, J. P. Epping, T. Hellwig, M. Hoekman, R. G. Heideman, P. J. M. van der Slot, C. J. Lee, R. Schmidt, R. Bratschitsch, C. Fallnich, and K.-J. Boller, Opt. Express **25**, 1542 (2017).
6. K. Saha, Y. Okawachi, B. Shim, J. S. Levy, R. Salem, A. R. Johnson, M. A. Foster, M. R. E. Lamont, M. Lipson, and A. L. Gaeta, Opt. Express **21**, 1335 (2013).
7. M. H. P. Pfeiffer, C. Herkommer, J. Liu, H. Guo, M. Karpov, E. Lucas, M. Zervas, and T. J. Kippenberg, Optica **4**, 684 (2017).
8. J. Joo, J. Park, and G. Kim, IEEE Photon. Technol. Lett. **30**, 740 (2018).
9. S. Chung, M. Nakai, and H. Hashemi, Opt. Express **27**, 13430 (2019).
10. L. Koehler, P. Chevalier, E. Shim, B. Desiatov, A. Shams-Ansari, M. Piccardo, Y. Okawachi, M. Yu, M. Loncar, M. Lipson, A. L. Gaeta, and F. Capasso, Opt. Express **26**, 34965 (2019).
11. G. Coppola, L. Sirleto, I. Rendina, and M. Iodice, Opt. Eng. **50**, 071112 (2011).
12. A. Arbabi and L. L. Goddard, Opt. Lett. **38**, 3878 (2013).
13. G. Cocorullo, F. G. Della Corte, and I. Rendina, Appl. Phys. Lett. **74**, 3338 (1999).
14. X. Zhou, S. Liu, H. Tang, Z. Zhong, and Y. Liu, Mod. Phys. Lett. B **30**, 1650161 (2016).
15. F. A. Memon, F. Morichetti, and A. Melloni, ACS Photon. **5**, 2755 (2018).
16. S. Habermehl, J. Appl. Phys. **83**, 4672 (1998).
17. C. Lacava, S. Stankovic, A. Z. Khokhar, T. D. Bucio, F. Y. Gardes, G. T. Reed, D. J. Richardson, and P. Petropoulos, Sci. Rep. **7**, 22 (2017).
18. C. J. Krückel, A. Fülöp, Z. Ye, P. A. Andrekson, and V. Torres-Company, Opt. Express **25**, 15370 (2017).
19. K. J. A. Ooi, D. K. T. Ng, T. Wang, A. K. L. Chee, S. K. Ng, Q. Wang, L. K. Ang, A. M. Agarwal, L. C. Kimerling, and D. T. H. Tan, Nat. Commun. **8**, 13878 (2017).
20. T. Wang, D. K. T. Ng, S.-K. Ng, Y.-T. Toh, A. K. L. Chee, G. F. R. Chen, Q. Wang, and D. T. H. Tan, Laser Photon. Rev. **9**, 498 (2015).
21. G.-R. Lin, S.-P. Su, C.-L. Wu, Y.-H. Lin, B.-J. Huang, H.-Y. Wang, C.-T. Tsai, C.-I. Wu, and Y.-C. Chi, Sci. Rep. **5**, 9611 (2015).
22. K. P. Lim, V. Krishnamurthy, J. F. Ying, J. Pu, and Q. Wang, IEEE Trans. Magn. **53**, 1 (2017).
23. H. Mäckel and R. Lüdemann, J. Appl. Phys. **92**, 2602 (2002).
24. A. C. Hryciw, R. D. Kekatpure, S. Yerci, L. Dal Negro, and M. L. Brongersma, Appl. Phys. Lett. **98**, 041102 (2011).
25. J. Teng, P. Dumon, W. Bogaerts, H. Zhang, X. Jian, X. Han, M. Zhao, G. Morthier, and R. Baets, Opt. Express **17**, 14627 (2009).
26. W. Bogaerts, P. De Heyn, T. Van Vaerenbergh, K. De Vos, S. Kumar Selvaraja, T. Claes, P. Dumon, P. Bienstman, D. Van Thourhout, and R. Baets, Laser Photon. Rev. **6**, 47 (2012).
27. F. Qiu, A. M. Spring, and S. Yokoyama, ACS Photon. **2**, 405 (2015).
28. C. W. Holzwarth, T. Barwicz, and H. I. Smith, J. Vac. Sci. Technol. B **25**, 2658 (2007).
29. G. Ghosh, Appl. Opt. **36**, 1540 (1997).
30. S. Knief and W. von Niessen, Phys. Rev. B **59**, 12940 (1999).
31. J. Bauer, Phys. Status Solidi A **39**, 411 (1977).
32. A. Arbabi, Y. M. Kang, C.-Y. Lu, E. Chow, and L. L. Goddard, Appl. Phys. Lett. **99**, 091105 (2011).